CORPUS PUBLISHERS

Journal of Mineral and Material Science (JMMS)

ISSN: 2833-3616

Volume 3 Issue 3, 2022

Article Information

Received date: Aug 25, 2022

Published date: Sep 27, 2022

*Corresponding author

Eduardo Ignacio Godoy Riveros, INGMAT R&D Centre, Jose Miguel de la Barra 412, 4to piso, Santiago, Chile

Keyword

Geomechanics; Axisymmetric; DtN Finite Element; Boussinesq Problem

Research Article

Accuracy of a DtN Finite Element Approach for the Elastic Half-Space

Mario Duran[1] and Eduardo Godoy[2*]

[1]*Departamento de Ingenieria Matematica, Universidad de Concepcion, Casilla 160-C, Concepcion, Chile*

[2]*INGMAT R&D Centre, Jose Miguel de la Barra 412, 4to piso, Santiago, Chile*

Abstract

In this work, the accuracy of a DtN finite element approach is numerically assessed. This procedure allows an efficient and accurate numerical solution of boundary-value problems of axisymmetric elasticity in semi-infinite domains. For this kind of problems, no explicit closed-form expression for the associated DtN map exists, so a suitable semi-analytical approximation of it, in series form, is used to impose exact boundary conditions on a semi-spherical artificial boundary. The procedure is tested by solving the classical Boussinesq problem, whose exact solution is known analytically. The computed numerical solution is compared to the analytical solution, achieving an excellent agreement between both solutions, both for displacements and stresses. The convergence of the analytical solution to the numerical solution is numerically demonstrated, in terms of artificial boundary location, series truncation order and finite element mesh size.

Introduction

When simulating numerically certain problems arising in geomechanics and soil mechanics, such as excavation stability in mining or civil engineering, the surrounding ground is often modelled as a half-space. The numerical approach to be used then needs to be able to deal in some way with unbounded domains. Several numerical methods with that feature exist [1]. Among them, a good alternative is the use of finite elements in combination with exact boundary conditions provided by the Dirichlet-to-Neumann map on an artificial boundary, that is, a DtN-FEM approach [2]. In general, this type of procedure can be applied as long as that an explicit, analytical closed-form expression for the DtN map exists. Such is the case for most exterior problems, that is, when the involved domain corresponds to the whole space minus some bounded region [3,4]. However, applying a DtN-FEM approach to solve a problem formulated in a half-space could be tricky, mainly due to the lack of closed-form expressions for the DtN map in most cases of interest, so some approximation of it becomes necessary [5, 6]. In a relatively recent research [7,8], the authors presented an axisymmetric DtN-FEM approach for the elastic half-space, based on a semi-analytical approximation in series form of the associated DtN map. Its coupling with the finite element scheme is carried out directly on the discretised variational formulation of the boundary-value problem [8], specifically on the boundary integral terms on a semi-spherical artificial boundary. The method exhibited an excellent performance in terms of speed, precision and robustness. Its accuracy was investigated by solving a benchmark problem with explicit analytical solution, proposed by the authors and based upon the same procedure to obtain the semi-analytical approximation to the DtN map. In this paper, the accuracy of the DtN-FEM approach is further assessed by solving the classical Boussinesq problem, consisting in the elastic response of a half-space subject to a vertical point load applied on its surface [9]. The numerical solution is then compared to the analytical solution, and the agreement between both solutions is investigated. The relative errors of displacements and stresses are analysed for different artificial boundary locations, series truncation orders and finite element mesh sizes. The convergence of the method in terms of these three parameters is numerically studied.

Overview of the DtN-FEM

In what follows, an overview of the DtN-FEM approach is given. Full details are found in [8]. Let us consider the lower half-space, described in cylindrical coordinates (ρ, θ, z) as the region in R^3 where $\rho \geq 0$ and $z < 0$, or alternatively in spherical coordinates (r, θ, φ) as the region in R^3 where $r > 0$ and $\pi/2 < \varphi < \pi$. Notice that this semi-infinite region is axisymmetric with respect to the z-axis, and in particular it does not depend on the azimuthal angle θ. The lower half-space will be described in cylindrical coordinates (ρ, z) or spherical coordinates (r, φ) as appropriate. The associated unit vectors are denoted by $(\hat{\rho}, \hat{z})$ and $(\hat{r}, \hat{\varphi})$, respectively. Let us denote by $u = (u_\rho, u_z)^T$ the displacement field and by $\varepsilon = (\varepsilon_\rho, \varepsilon_z, \varepsilon_\theta, \varepsilon_{\rho z})^T$ the strain tensor. In the axisymmetric case, ε has four components (cf. [10]), which are defined as

$$\varepsilon_\rho = \frac{\partial u_\rho}{\partial \rho}, \quad \varepsilon_z = \frac{\partial u_z}{\partial z}, \quad \varepsilon_\theta = \frac{u_\rho}{\rho}, \quad \varepsilon_{pz} = \frac{1}{2}\left(\frac{\partial u_\rho}{\partial z} + \frac{\partial u_z}{\partial \rho}\right) \tag{1}$$

The stress tensor $\sigma = (\sigma_\rho, \sigma_z, \sigma_\theta, \sigma_{\rho z})^T$ is given in terms of ε by the isotropic Hooke law. Its components are

$$\begin{aligned} \sigma_\rho &= \lambda(\varepsilon_\rho + \varepsilon_z + \varepsilon_\theta) + 2\mu\varepsilon_\rho, && (2a)\\ \sigma_z &= \lambda(\varepsilon_\rho + \varepsilon_z + \varepsilon_\theta) + 2\mu\varepsilon_z, && (2b)\\ \sigma_\theta &= \lambda(\varepsilon_\rho + \varepsilon_z + \varepsilon_\theta) + 2\mu\varepsilon_\theta, && (2c)\\ \sigma_{\rho z} &= 2\mu\varepsilon_{\rho z}, && (2d) \end{aligned} \tag{2}$$

where λ, μ are Lame's constants of the medium, which is also characterised by Young modulus E and Poisson ratio ν. Both pairs of elastic constants are linked by

$$\lambda = \frac{\nu E}{(1+\nu)(1-2\nu)}, \quad \mu = \frac{E}{2(1+\nu)} \tag{3}$$

The Boussinesq problem is stated in the axisymmetric case as follows: Find a displacement field u defined in the half-space, with values in R^2, such that

$$\begin{aligned} &\nabla \cdot \sigma = 0 && \text{in } \{\rho > 0, z < 0\}, && (4a)\\ &\sigma\hat{z} = -P\delta_0\hat{z} && \text{on } \{z = 0\}, && (4b)\\ &\sigma_{\rho z} = u_\rho = 0 && \text{on } \rho = 0, && (4c)\\ &|u| = O(r^{-1}) && \text{as } r \to \infty, && (4d) \end{aligned} \tag{4}$$

where in the right-hand of (4b), P is the point load magnitude and δ_0 stands for the Dirac delta distribution at the origin. The problem is completed with a boundary condition on the vertical axis (4c), which in order to preserve the axisymmetry must be constrained against horizontal displacement and free of shear traction, and a standard decaying condition at infinity for u (4d). The Boussinesq problem (4) has and analytical solution, which is exhibited later. To solve (4) with the DtN-FEM approach, a semi-spherical artificial boundary is used to truncate the half-space, dividing it into a bounded interior computational domain Ω and an unbounded exterior domain Ω^e, as indicated in Figure 1. The truncation radius is denoted by R. Notice that the artificial boundary, denoted by Γ_R, simply corresponds to a quarter of circumference. The vertical and horizontal boundaries of Ω are denoted by Γ_i and Γ_s, respectively, where the latter forms part of the vertical axis of rotational symmetry. The Boussinesq problem is then restated in Ω as follows: Find $u : \Omega \to R^2$ such that

$$\begin{aligned} &\nabla \cdot \sigma = 0 \text{ in } \Omega, && (5a)\\ &\sigma\hat{z} = -P\delta_0\hat{z} \text{ on } \Gamma_i, && (5b)\\ &\sigma_{\rho z} = u_\rho = 0 \text{ on } \Gamma_s, && (5c)\\ &\sigma\hat{r} = -Mu \text{ on } \Gamma_R, && (5d) \end{aligned} \tag{5}$$

where M denotes de DtN map of the elastic half-space, which for the moment is assumed to be known. To state a variational (or weak) formulation of (5), we consider the Sobolev space V consisting of physically admissible vector functions $v : \Omega \to R^2$, with both components v_ρ, v_z in $H^1(\Omega)$ and v_ρ with zero trace on Γ_s. The variational formulation of (5) reads: Find u V such that

$$a(u,v) + \int_{\Gamma_R} Mu \cdot v d\Gamma_R = f(v) \qquad \forall \upsilon \in V \tag{6}$$

where a corresponds to the bilinear form of axisymmetric linear elasticity and f is a linear operator related to external forces, in this case the vertical point load. The integral term accounts for the contribution of DtN map and corresponds to the non-standard part of the variational formulation.

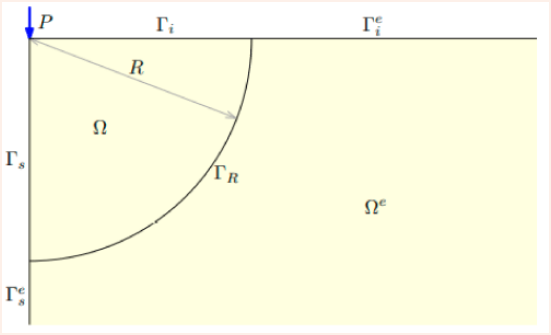

Figure 1: Truncated domain.

Let us consider a standard FEM discretisation of (6) using P_1 triangular elements. Given a triangular mesh of Ω, its size is denoted by h. The components of the discrete vector solution $u^h = \left(u_\rho^h, u_z^h\right)^T$ are then sought in a finite-dimensional space $V_h \subset V$ consisting of continuous, piecewise linear functions, whose dimension is denoted by N_h. The usual basis for V_h is composed by nodal shape functions $\{\psi_i\}_{i=1}^{N_h}$ such that $\psi_i = 1$ at node i and $\psi_i = 0$ at all node $j \neq i$. The solution is thus expressed as

$$u^h = \sum_{i=1}^{N_h} \left(d_{\rho i}\hat{\rho} + d_{zi}\hat{z}\right)\psi_i \tag{7}$$

where $d_{\rho i}$ and d_{zi} are the unknown nodal values associated with components u_ρ^h and of the discrete solution u^h, respectively. Substitution of (7) in (6) leads to its matrix form, expressed as

$$Kd = F, \tag{8}$$

where the right-hand side F comes from the discretisation of the right-hand side of (6) and d is a vector containing the unknown coefficients $d_{\rho i}$, d_{zi}. The matrix of the system is written as:

$$K = K^a + K^b, \tag{9}$$

where K^a comes from the discretisation of the bilinear form a and K^b is related to the integral term in (6). Matrix K^a and vector F are computed by Gauss numerical integration, whereas the evaluation of matrix K^b requires a special procedure. This matrix has size $2N_h$, and is defined by blocks as

$$K^b = \begin{bmatrix} K^b_{\rho\rho} & K^b_{\rho z} \\ K^b_{z\rho} & K^b_{zz} \end{bmatrix} \tag{10}$$

These four blocks are defined through their ij-components as

$$\left[K^b_{\alpha\beta}\right]_{ij} = \int_{\Gamma_R} \psi_i \hat{\alpha} \cdot M\psi_j \hat{\beta} d\Gamma_R \qquad \alpha, \beta = \rho, z, \tag{11}$$

which are nonzero only if both nodes i and j lie on the artificial boundary Γ_R. Therefore, and recalling that there is no explicit closed-form expression for the DtN map M, highly accurate numerical approximations of terms $M\psi_j\hat{\rho}$ and $M\psi_j\hat{z}$, for every node j lying on Γ_R, are required in order to fully solve the boundary-value problem (5). To produce such approximations, we start by giving the mathematical DtN map definition. Given any displacement v ∈V, with trace $v \mid \Gamma_R \in \left[H^{1/2}\left(\Gamma_R\right)\right]^2$, we define $M\upsilon = -\sigma\hat{r} \mid \Gamma_R \in \left[H^{-1/2}\left(\Gamma_R\right)\right]^2$, where σ is the stress tensor whose components are computed through (1) and (2) from the displacement u, the solution of the following boundary-value problem stated in the exterior domain: Find $u : \Omega^e \to R^2$ such that:

$$\begin{aligned} &\nabla \cdot \sigma = 0 \quad in\ \Omega^e && \text{(12a)} \\ &\sigma\hat{z} = 0 \quad on\ \Gamma_i^e && \text{(12b)} \\ &u = v \quad on\ \Gamma_R && \text{(12c)} \\ &\sigma_{\rho z} = u_\rho = 0 \quad on\ \Gamma_s^e && \text{(12d)} \\ &|u| = O\left(r^{-1}\right) \quad as\ r \to \infty && \text{(12e)} \end{aligned} \tag{12}$$

which needs to be solved for $\upsilon = \psi_j\hat{\rho}$ and $\upsilon = \psi_j\hat{z}$. The technique to do so, fully described in [7,8], is based upon an enhanced version of the solution originally proposed by Eubanks [11]. By using Papkovich-Neuber potentials and separation of variables in spherical coordinates (r, φ), it is possible to find a general analytical solution to (12) in series form, which is expressed as

$$u(r,\phi)=\sum_{n=0}^{\infty}A_n\left(\frac{R}{r}\right)^{2n+2}\omega_n^{(A)}(\phi)+\sum_{n=-1}^{\infty}B_n\left(\frac{R}{r}\right)^{2n+3}\omega_n^{(B)}(\phi) \tag{13}$$

where the vector functions $\omega_n^{(A)}(\cdot)$ and $\omega_n^{(B)}(\cdot)$ are known and coefficients A_n and B_n are arbitrary. The associated stress tensor σ is written as

$$\sigma(r,\phi)=\frac{1}{R}\left[\sum_{n=0}^{\infty}A_n\left(\frac{R}{r}\right)^{2n+3}\tau_n^{(A)}(\phi)+\sum_{n=-1}^{\infty}B_n\left(\frac{R}{r}\right)^{2n+4}\tau_n^{(B)}(\phi)\right] \tag{14}$$

where the tensor functions $\tau_n^{(A)}(.)$ and $\tau_n^{(B)}(.)$ are known. This solution, in its series form (13)-(14), satisfies (12a), (12b), (12d) and (12e). In order for it to satisfy (12c), coefficients A_n and B_n needs to be determined as a function of the Dirichlet datum v. This is not possible in a fully analytical way, so it is done numerically. To that purpose, we define the following quadratic energy functional J:

$$J(u)=-\frac{1}{2R}\int_{\Gamma_R}\sigma\hat{r}\cdot u\,d\Gamma_R+\frac{1}{R}\int_{\Gamma_R}\sigma\hat{r}\cdot\upsilon\,d\Gamma_R \tag{15}$$

which is positive definite (notice that the unit normal vector pointing outwards Ω^e corresponds to $-\hat{r}$) and reaches its minimum when (12c) holds. Substituting (13)-(14) in (15), with the series truncated at a finite order N and expanding, we arrive at a quadratic form, which is expressed as

$$J(x)=\frac{1}{2}x^TQx-x^Ty \tag{16}$$

where x is a vector containing coefficients A_n, B_n up to the truncation order N, Q is a symmetric and positive definite matrix containing integrals of products between functions $\omega_n^{(A)}$, $\omega_n^{(B)}$ and $\tau_n^{(A)}$, $\tau_n^{(B)}$ and y is a vector containing integrals of products between functions $\tau_n^{(A)}$, $\tau_n^{(B)}$ and v. The entries of matrix Q are computed analytically, and the components of vector y are computed by Gauss numerical integration for $v=\psi_j\hat{\rho}$, $\psi_j\hat{z}$. The quadratic functional J in (16) reaches its minimum when x satisfies the linear system Qx = y, which is solved by exploiting the block structure of Q, in such a way that the coefficients A_n and B_n are in practice computed by simple forward and backward substitutions. This procedure allows us to evaluate the entries of matrix K^b given in (11), and thus to fully solve the boundary value problem (5). Numerical experiments are presented in the next section.

Numerical Experiments

The analytical solution of the Boussinesq problem (4) is provided next. The components of the displacement field u are given by

$$u_\rho(\rho,z)=-\frac{P\rho}{4\pi\mu r}\left(\frac{z}{r^2}+\frac{1-2\nu}{r-z}\right) \tag{17a}$$

$$u_z(\rho,z)=-\frac{P}{4\pi\mu r}\left(2(1-\nu)+\frac{z^2}{r^2}\right) \tag{17b}$$

and the component of the stress tensor σ are given by

$$\sigma_\rho(\rho,z) = -\frac{P}{2\pi r^2}\left(\frac{3\rho^2 z}{r^3} - (1-2\nu)\left(\frac{z}{r}+\frac{r}{r-z}-\frac{\rho^2(2r-z)}{r(r-z)^2}\right)\right), \quad (18a)$$

$$\sigma_\theta(\rho,z) = -\frac{(1-2\nu)P}{2\pi r^2}\left(\frac{z}{r}+\frac{r}{r-z}\right), \quad (18b)$$

$$\sigma_z(\rho,z) = \frac{3Pz^3}{2\pi r^5} \quad (18c)$$

$$\sigma_{\rho z}(\rho,z) = \frac{3P\rho z^3}{2\pi r^5} \quad (18d)$$

The procedure described in the previous section was thus applied to the Boussinesq problem. Triangular meshes of the domain Ω, depicted in Figure 1, were generated for different radii R. As the solution to the Boussinesq problem has a singularity at the origin, the point load cannot be directly applied to a single mesh node in the numerical implementation. To approximate numerically such singularity, the point load is instead distributed along a small segment of length d << R, at which a smaller mesh size needs to be set. An example of mesh is presented in Figure 2, for a radius R = 5 m and a segment length d = 0.1 m (indicated in red). The whole mesh is presented on the left, and a zoom-in on the origin is shown on the right. The local mesh size was set to 0.15 m on Γ_R, and to 0.01 m on the small segment at the origin.

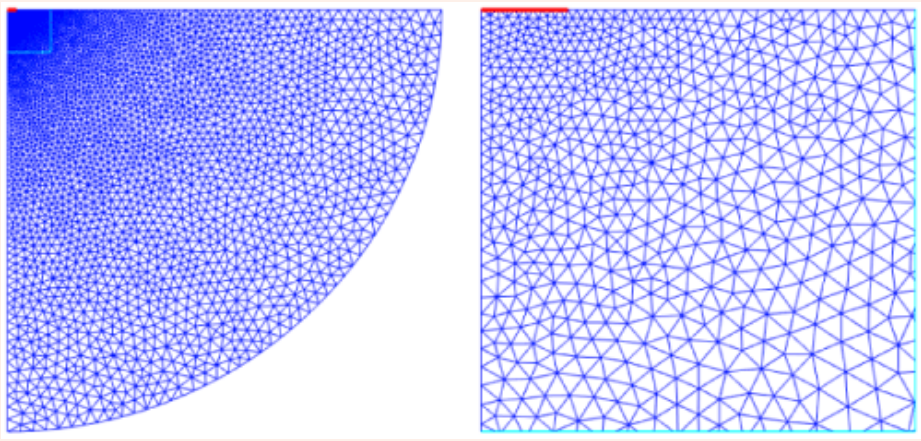

Figure 2: Example of mesh: whole mesh (left) and zoom-in on the origin (right).

To make a preliminary verification of the DtN-FEM accuracy, a numerical example was simulated for an elastic medium with Young's modulus E = 80 GPa and Poisson's ratio ν = 0.25. A point load magnitude P = 40 GPa was assumed. Given a radius R = 5 m, a mesh was generated, with the local mesh size set to h = 0.01 m at the origin and to h = 0.1 m on Γ_R. The infinite series were truncated at N = 40. Comparisons of displacement components uρ and uz are provided in Figures 3 & 4, respectively. In both cases, the analytical solution, evaluated in the mesh, is presented on the left, whereas the numerical DtN-FEM solution is presented on the right. These four plots cover a square region in the (ρ, z)-plane defined by 0 m ≤ ρ ≤ 3 m and −3 m ≤ z ≤ 0 m. It is observed that the numerical solution approximates the analytical solution correctly. Some minor discrepancies arise at the origin, due to the numerical approximation of the singularity.

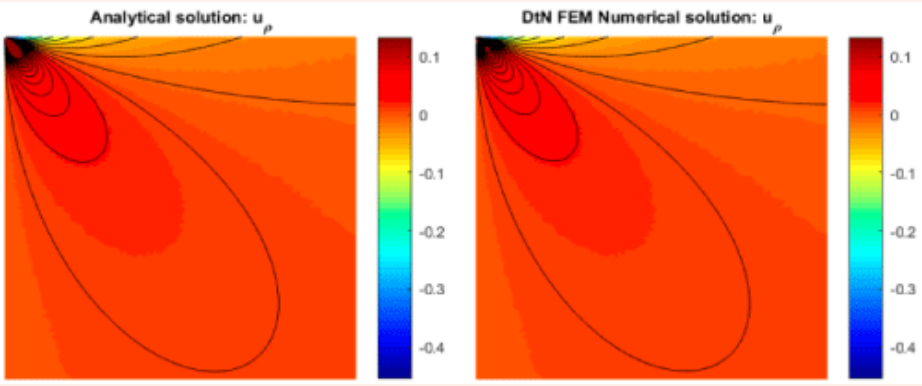

Figure 3: Comparison of displacement component up: analytical (left) and numerical (right).

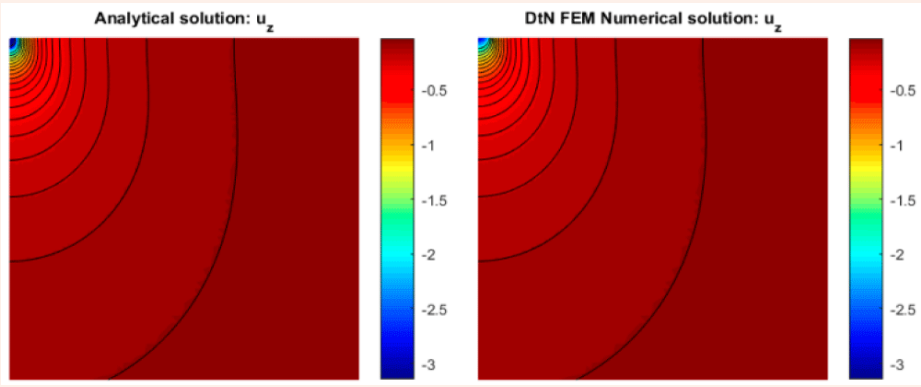

Figure 4: Comparison of displacement component uz: analytical (left) and numerical (right).

In order to study numerically the convergence of the DtN-FEM approach, the L^2-relative error on the artificial boundary Γ_R is utilised. Given a displacement field $u^h = \left(u_\rho^h, u_z^h\right)^T$, numerically computed in a mesh of size h > 0, and the analytical displacement $u = \left(u_\rho, u_z\right)^T$ defined in (17), the L^2-relative error associated with each displacement component is defined as

$$E\left(u_\alpha^h\right) = \frac{\| u_\alpha - u_\alpha^h \|_{0,\Gamma_R}}{\| u_\alpha \|_{0,\Gamma_R}} \quad , \alpha = \rho, z \tag{19}$$

where $\| \cdot \|_{0,\Gamma_R}$ stands for the scalar L^2-norm on Γ_R, defined as

$$\| \upsilon \|_{0,\Gamma_R} = \left(\int_{\Gamma_R} |\upsilon|^2 \, d\Gamma_R \right)^{1/2} \tag{20}$$

for any scalar function $\upsilon \in L^2\left(\Gamma_R\right)$. The L²-relative error associated with the whole displacement u^h is also considered, which is defined as

$$\| \upsilon \|_{0,\Gamma_R} = \left(\| \upsilon_\rho \|^2_{0,\Gamma_R} + \| \upsilon_z \|^2_{0,\Gamma_R} \right)^{1/2} \tag{21}$$

where this time, $\| \cdot \|_{0,\Gamma_R}$ denotes the vector L²-norm on Γ_R, that is,

$$\| \upsilon \|_{0,\Gamma_R} = \left(\| \upsilon_\rho \|^2_{0,\Gamma_R} + \| \upsilon_z \|^2_{0,\Gamma_R} \right)^{1/2} \tag{22}$$

for any vector function v with components $\upsilon_\rho, \upsilon_z \in L^2\left(\Gamma_R\right)$. The L²-relative error of stress on Γ_R is also analysed. The numerical stress $\sigma^h = \left(\sigma^h_\rho, \sigma^h_z, \sigma^h_\theta, \sigma^h_{\rho z}\right)^T$ is computed from the numerical displacement u^h, by first evaluating strain components through (1), with the displacement derivatives computed by numerical derivation on the mesh, and then by evaluating stress com- ponents through (2). The analytical stress $\sigma = \left(\sigma_\rho, \sigma_z, \sigma_\theta, \sigma_{\rho z}\right)^T$, on the other hand, is given by (18). The L²-relative errors associated with each stress component and the whole stress σ^h, denoted respectively by $E\left(\sigma^h_\alpha\right)\left(\alpha = \rho, z, \theta, \rho z\right)$ and $E(\sigma^h)$, are defined in analogous way to (19) and (21), respectively. In the convergence studies that follow, the same elastic parameter values E = 80 GPa and ν = 0.25 were kept, as well as the point load magnitude P = 40 GPa. Firstly, we studied numerically the convergence in terms of the radius R, which determines the artificial boundary location. To that purpose, a set of 20 decreasing radius values was defined as follows: $R_1 = 30$ m and $R_{i+1} = 0.9R_i$, for i = 1, . . . , 19. For each one of them, a mesh was generated, keeping the local mesh size set to h = 0.01 m at the origin and to h = 0.15 m on Γ_R, independently of the value of R. For the numerical solution, the infinite series were truncated at N = 40 in all the cases. The computed relative errors in function of R are presented in loglog-scale, in which the chosen radius values are equispaced. Figure 5 presents separate plots with the L²-relative error curves of each displacement component (left) and stress component (right). Figure 6 shows a single plot with the L²-relative error curves of the whole displacement field and stress tensor. It is observed that the relative error decreases as the radius increases. This is explained by the fact that as the artificial boundary is placed at an increasing distance from the origin, the singularity generated by the point load has a decreasing influence on the numerical solution evaluated at Γ_R. In the case of the displacement field, which is directly the solution of (5), the relative errors of each component remain below 0.1%, which further demonstrates the accuracy of the DtN-FEM approach. For the largest considered radius, R = 30 m, the relative error of displacement is about 0.0024%. In addition, and as expected, the relative error of stresses is larger than that of displacements, mainly since the stress tensor is not directly the solution of (5), but it depends on displacement derivatives, which are computed through numerical derivation on the mesh. For the largest considered radius, R = 30 m, the relative error of stress is about 1.4%. Moreover, it is clearly observed that the relative error curves shown in Figures 5 & 6 are nearly straight lines in loglog-scale. Their respective approximate slopes were computed by linear regression and the resulting values are presented in Tables 1 & 2 for displacement (vector and its components) and stress (tensor and its components), respectively. The slope of displacement error curves is nearly −2, whereas that of stress error curves is nearly −1, which provides strong numerical evidence that the convergence of our DtN-FEM approach, in terms of artificial boundary location R, is of second order.

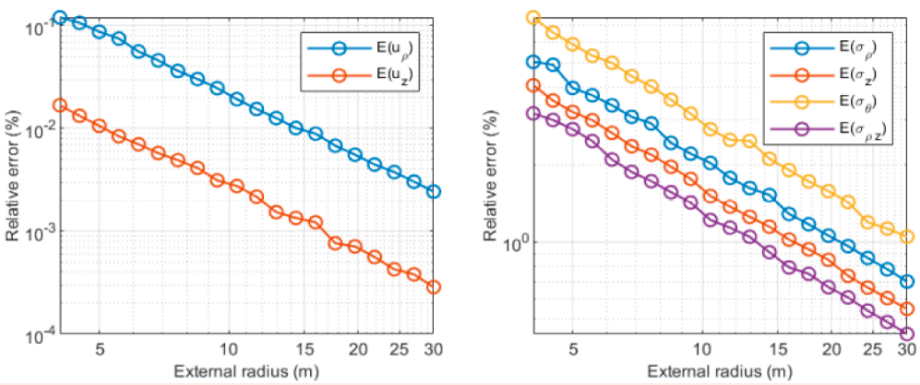

Figure 5: L^2-relative error curves in function of R by components: displacement (left) and stress (right).

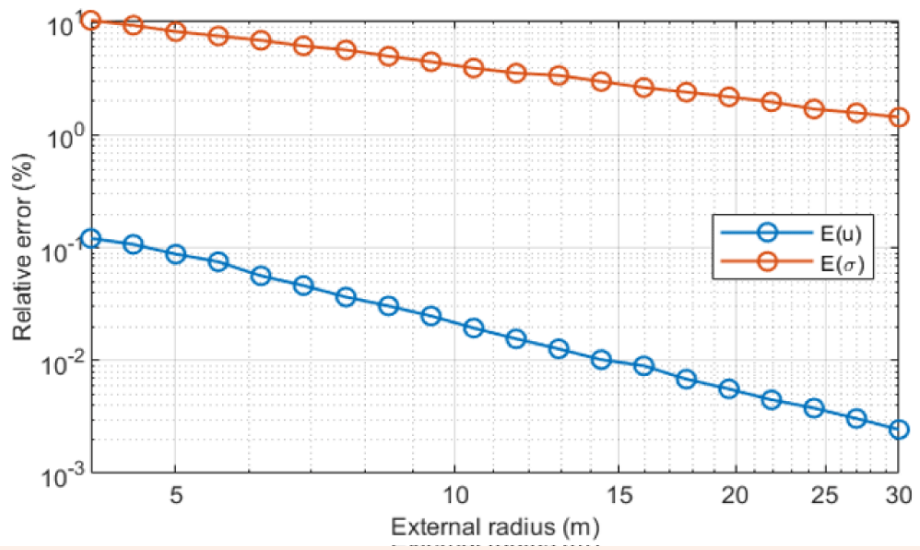

Figure 6: Displacement field and stress tensor L^2-relative error curves in function of R.

Table 1: Approximate slopes of displacement L^2-relative error curves in function of R.

Displacement (Vector or Component)	u	u_ρ	u_z
Approximate slope	−1.9738	−1.9735	−1.9904

Table 2: Approximate slopes of stress L^2-relative error curves in function of R.

Stress (Tensor or Component)	σ_ρ	σ_ρ	σ_z	σ_θ	$\sigma_{\rho z}$
Approximate slope	−0.9923	−0.9962	−0.9918	−0.9839	−1.0245

Secondly, we studied numerically the convergence in terms of the mesh size h. The artificial boundary location was set to R = 10 m and a set of 20 decreasing mesh sizes was defined as follows: $h_1 = 0.5$ m and $h_{i+1} = 0.9h_i$, for i = 1, . . . , 19. The local mesh size on Γ_R was set to each one of these values and meshes were generated, with the local mesh size at the origin set to h = 0.01 m in all the cases. For the numerical solution, the infinite series were truncated again at N = 40. The computed relative errors in function of h are presented again in loglog-scale, in which the chosen mesh size values are equispaced. Figure 7 presents separate plots

containing the L^2-relative error curves of each displacement component (left) and stress component (right). Figure 8 includes a single plot with the L^2-relative error curves of the whole displacement field and stress tensor. It is observed that the relative error decreases as h decreases, just as expected. A finer mesh size results in a better numerical approximation of the analytical solution. For the displacement field, the computed relative errors of its components remain inferior to 0.02% for the values of h considered, which further confirms the precision of the method. For the smallest mesh size, the whole displacement field has a relative error of 0.0038%. On the other hand, a larger stress relative error is again obtained, which is explained by the same reasons as the previous convergence study in terms of R. Furthermore, it is noticed from Figures 7 & 8 that, once again, the relative error curves correspond to nearly straight lines in loglog-scale. Their approximate slopes, computed by linear regression, are presented in Tables 3 & 4 for displacement (vector and its components) and stress (tensor and its components), respectively. The slope of displacement error curves is nearly 2, and that of stress error curves is nearly 1. This fact gives strong numerical evidence that the convergence of this DtN-FEM approach, in terms of the mesh size h, is of second order, which reinforces what had been found in the previous research [8].

Table 3: Approximate slopes of displacement L^2-relative error curves in function of h.

Displacement (Vector or Component)	u	u_ρ	u_z
Approximate slope	1.9729	1.9723	1.9864

Table 4: Approximate slopes of stress L^2-relative error curves in function of h.

Stress (Tensor or Component)	σ	σ_ρ	σ_z	σ_θ	$\sigma_{\rho z}$
Approximate slope	0.9837	0.9982	0.9889	0.9690	1.0357

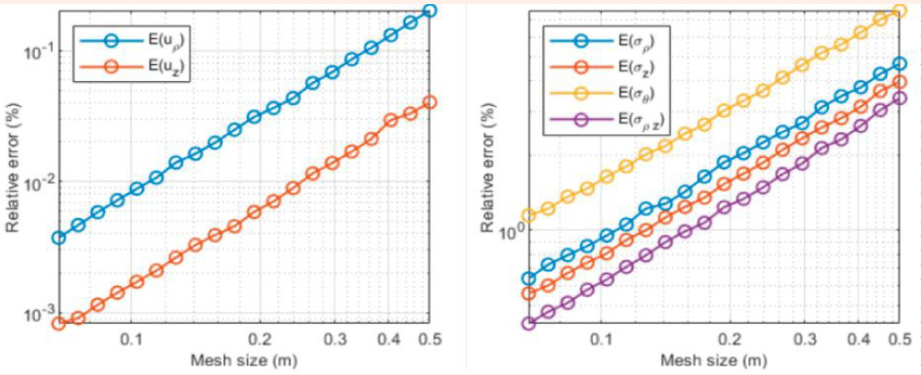

Figure 7: L^2-relative error curves in function of h by components: displacement (left) and stress (right).

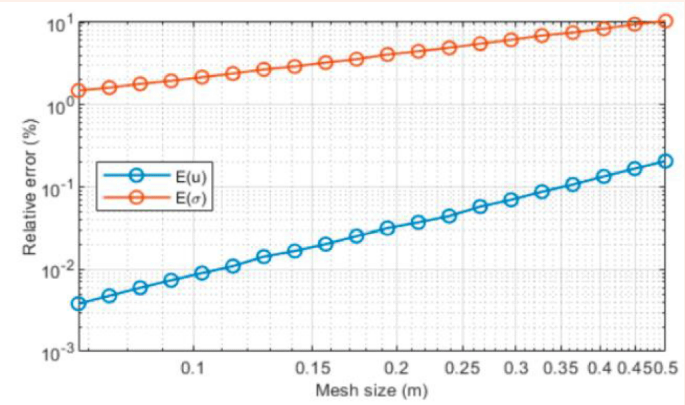

Figure 8: Displacement field and stress tensor L^2-relative error curves in function of h.

Finally, we analysed numerically the convergence in terms of the series truncation order N . For this, a single mesh was employed, with a radius of R = 10 m, and local mesh sizes of h = 0.01 m at the origin and h = 0.15 m on Γ_R. The truncation order was varied from N = 2 to N = 200, with increments of ΔN = 2. Figure 9 presents separately the L^2 relative error curves of displacement components (left) and stress components (right), this time in linear scale. We note that, even if the relative error of displacement decreases with increasing truncation order, just as expected, N has little influence on it. A higher dependance is observed at low values of N, however, the curve tends to a constant value for higher values of N. Moreover, both displacement components have small relative errors, their values are at most 0.03%. In the case of the stress components, the dependance of relative error on N is even less significant. In fact, nearly constant values are obtained. And as usual, these values are greater than those of displacement relative error. Therefore, this DtN-FEM approach is robust, since even for low series truncation order, precise results are obtained.

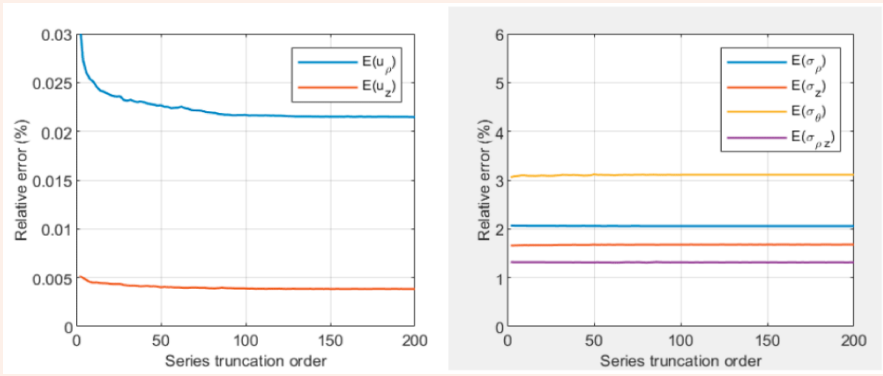

Figure 9: L^2-relative error curves in function of N by components: displacement (left) and stress (right).

Concluding Remarks

The accuracy of a DtN-FEM approach for the axisymmetric elastic half-space has been demonstrated by solving the Boussinesq problem, a classical benchmark problem of elasticity whose exact solution is known analytically. The numerical solution shows an excellent agreement with the analytical one. The numerical results presented show that the numerical approach approximates the correct solution of the Boussinesq problem. In particular, this approach is able to compute accurately the solution on a semi-spherical artificial boundary that truncates the half-space in an arbitrary location. The numerical evidence shows that the convergence of this method is of second order, both in terms of the artificial boundary location R and the mesh size h. Moreover, the method shows robustness with respect to the series truncation order N , as it computes accurate results even for low values of N . Thanks to these advantages, the proposed DtN-FEM approach shows high potentiality to be applied to certain problems arising in geomechanics and soil mechanics, as allows for reducing the computational domain size and therefore, improving the computation time.

Acknowledgement

The authors acknowledge the helpful suggestions of Juan David Rayo and Marıa Teresa Zandarin from JRI Ingenierıa S.A., which made it possible to generate valuable instances of validation of the practical numerical approach employed in this work.

References

1. Givoli D (1992) Numerical methods for problems in infinite domains. Elsevier, Amsterdam, Netherlands.
2. Givoli D (1999) Recent advances in the DtN FE method. Arch Comput Method E 6(2): 71-116.
3. Givoli D, Keller JB (1989) Special finite elements for use with high-order boundary conditions. Comput Methods Appl Mech Engrg 119(3-4): 199-213.
4. Han HD, Zheng CXJ (2005) Artificial boundary method for the three-dimensional exterior problem of elasticity. Comput Math 23: 603-618.
5. Givoli D, Vigdergauz S (1993) Artificial boundary conditions for 2D problems in geophysics. Comput Methods Appl Mech Engrg 110(1-2): 87-101.
6. Han H, Bao W, Wang T (1997) Comput Methods Appl Mech Engrg 147: 369-385.

7. Boccardo V, Godoy E, Duran M (2015) An efficient semi-analytical method to compute displacements and stresses in an elastic half-space with a hemispherical pit. Adv Appl Math Mech 7(3): 295-322.

8. Godoy E, Boccardo V, Duran MJ (2017) A dirichlet-to-neumann finite element method for axisymmetric elastostatics in a semi-infinite domain. Comput Phys 328: 1-26.

9. Podio-Guidugli P, Favata A (2014) Elasticity for geotechnicians: A modern exposition of Kelvin, Boussinesq, Flammant, Cerrutti, Melan and Mindlin Problems. 204 of Solid Mechanics and Its Applications. Springer, Germany.

10. Sadd MH (2005) Elasticity: theory, applications, and numerics. Elsevier Butterworth- Heinemann, Boston, US.

11. Eubanks RA (1954) Stress concentration due to a hemispherical pit at a free surface. J Appl Mech 21(1): 57-62.